



**Moiré-Templated Strain Patterning in Transition-Metal  
Dichalcogenides and Application in Twisted Bilayer MoS<sub>2</sub>**

Journal:	<i>Nanoscale</i>
Manuscript ID	NR-ART-08-2018-006269.R1
Article Type:	Paper
Date Submitted by the Author:	25-Oct-2018
Complete List of Authors:	Zhu, Shuze; UIUC, Mechanical Johnson, Harley; University of Illinois at Urbana-Champaign,

SCHOLARONE™  
Manuscripts

# Moiré-Templated Strain Patterning in Transition-Metal Dichalcogenides and Application in Twisted Bilayer MoS<sub>2</sub>

Shuze Zhu<sup>†</sup> and Harley Johnson\*

Department of Mechanical Science and Engineering

University of Illinois at Urbana-Champaign, Urbana, IL 61801, USA

**Abstract:** To take full advantage of the electronic properties of transition-metal dichalcogenides and their vdW layered structures, it will be necessary to control the local electronic structure, on which the effect of lattice deformation is significant. Nevertheless, a general approach to programming nanoscale morphology in TMD materials, which would permit local strain engineering, has proven elusive. In this work, we propose a general moiré-templated nanoscale morphology engineering method based on bilayer TMDs. The moiré superlattice plays the key role in enforcing in-plane periodical variations in local interlayer spacing and potential energy. Upon global in-plane compression, the high-energy, large-interlayer-separation stacking domains serve as periodic buckling initiation sites. The buckled features can be thus precisely correlated to the moiré periodicity. The spatial profile of the buckled morphology and strain field are possible to be pre-determined, providing a bridge to the electronics and optoelectronics design. We take twisted bilayer MoS<sub>2</sub> to demonstrate our approach. We further demonstrate how the morphology can modulate band gap and optical absorption of an MoS<sub>2</sub> monolayer, envisioned as a potential constituent layer in a Moiré-templated, strain-engineered vdW heterostructure of TMDs. The robustness and programmable nature of our approach arise from superlattice symmetry, energetics and mechanics. Our approach provides a new strategy for on-demand design of morphology and local strain in TMDs under mechanical deformation.

**Keywords:** transition-metal dichalcogenides, MoS<sub>2</sub>, Moiré, morphology engineering, strain engineering

<sup>†</sup> S.Z. (shuzezhu@illinois.edu).

\* H.J. (htj@illinois.edu).

## 1. Introduction

The electronic structure of transition-metal dichalcogenides (TMDs) is tied to their lattice configuration, and thus to morphology and strain. Because TMDs can sustain large elastic deformation, strain engineering, or more generally, morphology engineering, is a promising approach to tune the structural and electronic properties of TMDs. For example, morphology-strain engineered TMD membranes exhibit spatially varying band gaps which allow harvesting of solar photons over a wider energy range. It is found that local strain can engineer the confinement potentials for excitons with possibilities for efficient collection of solar energy.<sup>1</sup> In molybdenum disulphide ( $\text{MoS}_2$ ), local band gap and exciton energy decrease continuously as local strain increases.<sup>1-3</sup> Given sufficiently large exciton binding energies, the decreasing exciton energy profile will drive exciton to motion towards the smaller gap region, where efficient charge extraction can be designed.<sup>1</sup> This mechanism can effectively funnel broad-spectrum photon energy; the key is the strain-engineered spatially varying band energy profile. Experimental realization of this funneling effect has been demonstrated in strain-textured monolayer  $\text{MoS}_2$  deposited on a nanocone-patterned  $\text{SiO}_2$  substrate.<sup>4</sup> Nevertheless, nanoscale patterning techniques such as nanosphere lithography<sup>5</sup> are needed in order to obtain such strain profiles. Another experimental realization is achieved by inducing wrinkled atomically thin  $\text{MoS}_2$  layers on pre-stretched elastomeric substrate upon relaxation.<sup>6</sup> However, such a straining technique, though popular, lacks control on the distribution and shape profile of these wrinkles, which poses significant challenges to the precise control of TMD electronic properties.

TMDs and van der Waals' (vdW) structures comprising TMDs have significant potential for exotic applications and discovery of fundamental physics.<sup>7</sup> For example, recently there has been significant experimental progresses in systematic exfoliation and synthesis of multilayered TMDs using aromatic intercalants and Alkali metal cations, where promising electrocatalytic properties and exotic ferromagnetic behaviors have been identified and explained.<sup>8-10</sup> There are many constituent monolayer TMDs to choose from in constructing a layered vdW structure,<sup>11</sup> while still maintaining the mechanical flexibility within each layer. More importantly, the optoelectronic phenomena among homogeneous and heterogeneous multilayered TMDs are rich. Full exploration of the optoelectronic properties of TMDs and their vdW layered structures requires the ability to engineer the local electronic structure, for which the effects of lattice deformation and other factors like morphological symmetry are significant. For example, inversion asymmetry of monolayer TMDs is important in optoelectronic valleytronics.<sup>12, 13</sup> Naturally-stacked (2H stacking) bilayer MoS<sub>2</sub> acquires inversion symmetry, which would be an obstacle to applications in valleytronics if not for techniques such as electric bias<sup>14</sup> and mechanical bending<sup>15</sup>. The former breaks the inversion symmetry by perturbing the electron density through application of a perpendicular electric field,<sup>14</sup> and the latter through an imposing local bending deformation which morphologically guarantees inversion asymmetry.<sup>15</sup> It is suggested that each bent layer effectively behaves as an independent monolayer so that the distinct valleys in distinct layers can be excited independently.<sup>15</sup> Nevertheless, a practical approach to achieving controlled bending remains elusive, even though morphology and local strain engineering for vdW heterostructures of TMDs are simplified by the fact that each TMD monolayer maintains

its own direct band structure.<sup>16-18</sup> As a result, morphology-strain engineered optical functionality (e.g., absorption coefficients) is expected to sum up over each monolayer.<sup>19</sup> In addition, most vdW heterostructures of TMDs have type-II band alignment, where the optical active states of the top valence and bottom conduction bands are localized on different monolayers,<sup>16, 20-26</sup> allowing the electrons and holes to reside at different layers and thus longer lifetimes, which is crucial for photovoltaic devices. Since tuning local strain in vdW heterostructures of TMDs can shift band edges of different monolayers, a programmable nanoscale morphology and local strain engineering approach is highly desirable for opening up possibilities for unconventional device design.

In this article, we demonstrate theoretically and computationally a general approach to programmable nanoscale morphology engineering of moiré-patterned bilayer TMDs supported by a substrate, using twisted bilayer MoS<sub>2</sub> as an example. The approach is a step towards nanoscale morphology and strain programming of multilayer TMDs. With lattice mismatch or rotational alignment between layers, a periodic variation of atomic registry between individual van der Waals layers occurs, resulting in a moiré pattern or in-plane superlattice with a well-defined periodicity. Recently simulations suggest that manipulating the lattice mismatch results in varying moiré patterns in MoS<sub>2</sub> bilayer flakes on substrate.<sup>27</sup> To date, moiré patterns in two-dimensional materials have been used to modulate electronic structure, since different stacking patterns have distinct optical and electronic properties.<sup>28-31</sup> For example, the contrast in the band gaps of neighboring stacking domains can lead to tunable exciton funnelling.<sup>32</sup> Other emerging condensed matter phenomena such as topological moiré minibands,<sup>33-37</sup> topological insulator superstructures,<sup>38</sup> and superconducting states<sup>39</sup> have also been reported. Nevertheless,

much less attention has been given to how the varying interlayer coupling from moiré can be coupled with the morphology of the 2D layers under mechanical deformation. Given the significance of the coupling between electronic structure, morphology and strain, we introduce the concept of moiré-templated morphology engineering of bilayer TMDs. The robustness and programmable flavor of our approach arises from moiré symmetry, energetics, and mechanics. Our approach provides a new means to design morphology and local strain in TMDs via mechanical loading.

## 2. Results and Discussion

First, the approach requires forming a unit cell from commensurate stacking of the bilayer TMDs, compatible with the moiré symmetry. Figure 1(a) shows the geometry used to construct the unit cell. Each TMD monolayer has hexagonal lattice symmetry. To form a commensurate bilayer unit cell, geometrical symmetry requires that one lattice vector  $\vec{L}_1$  satisfy the constraint  $\vec{L}_1 = m\vec{a}_1^{(1)} + n\vec{a}_2^{(1)} = p\vec{b}_1^{(2)} + q\vec{b}_2^{(2)}$ , where  $m, n, p, q$  are integers, and  $\vec{a}_1^{(1)}, \vec{a}_2^{(1)}, \vec{b}_1^{(2)}, \vec{b}_2^{(2)}$  represent the properly relaxed lattice vectors from each TMD monolayer.<sup>40, 41</sup> The relaxation of lattice vectors might be necessary in order to allow a solution of  $m, n, p, q$  and  $\vec{L}_1$ . Relaxation also occurs within each layer in order to minimize the energy of atomic registry between layers. Another unit cell lattice vector,  $\vec{L}_2$  is then the rotation of  $\vec{L}_1$  by 60 degrees. The twisted angle  $\theta$  is then the angle between  $\vec{a}_1^{(1)}$  and  $\vec{b}_1^{(2)}$  (or  $\vec{a}_2^{(1)}$  and  $\vec{b}_2^{(2)}$ ). We note that the twisted angle  $\theta$  is a general notation and it can be zero. The bilayer unit cell therefore has two equal-length lattice vectors, and we denote this length as  $|\vec{L}_1| = |\vec{L}_2| = L$ . The above geometrical argument generally

works for both homogeneous and heterogeneous TMD bilayers, as long as the bilayer unit cell can be identified.

The unit cell is then a parallelogram (Figure 1(a)) with four sides of equal length  $L$  and internal angles of 60 or 120 degrees. As a result, there are two applicable unit cells (Figure 1(b)). The overlapping of the supercell constructed from these two unit cells allows us to further identify the translational periodical distribution of stacking domains. As a result, we can assign three high-symmetry stacking domains (labeled #1, #2, and #3) and three transitional stacking domains (labeled #4, #5, and #6). The transitional stacking domains serve as boundaries between the high-symmetry stacking domains. If the interlayer spacing (coupled to the potential energy density in the vdW layered system) of stacking domain #1 is the largest (Figure 1(c)), then mechanically the periodical arrays of stacking domains #1 are effective morphological perturbations for out-of-plane buckling. More importantly, the periodicity of such perturbations coincides with the unit cell of the moiré of the bilayer. Therefore, such well-defined perturbations can be used as controlled buckling initiation sites in substrate-supported moiré-patterned TMD bilayers when an in-plane compression is applied (Figure 1(d)). We will then show that such periodical morphological perturbations are guaranteed to exist in moiré patterns either from lattice mismatch or twist between TMD layers, making this observation generally applicable to a wide range of homogeneous or heterogeneous bilayer TMDs.

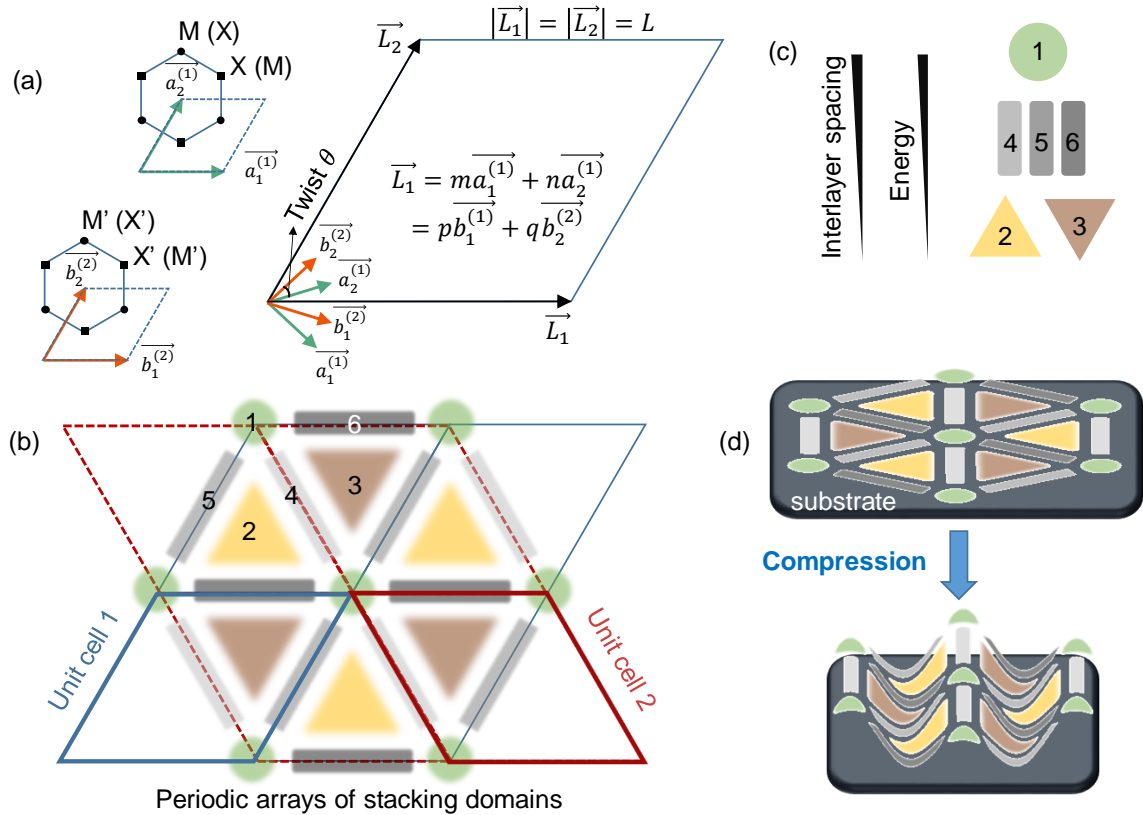


Figure 1: (a) Formation of unit cell from commensurate stacking of homogeneous or heterogeneous bilayer TMDs. Each TMD monolayer has hexagonal lattice symmetry. Symmetry requires that the unit cell of bilayer TMD is a parallelogram with four sides of equal length  $L$  and internal angles of 60 or 120 degrees. The twisted angle  $\theta$  is a general notation and can be zero. (b) Two choices of unit cell indicated by thick solid blue line and thick dashed red line can be identified in the supercell geometry (thin solid blue line and thin dashed red line). By translational symmetry one can assign three high-symmetry stacking domains (labeled #1, #2 and #3) and three transitional stacking domains (labeled #4, #5 and #6). (c) The condition at which the stacking domains #1 can serve as the morphological perturbations for out-of-plane buckling. (d) Schematic showing that the periodical arrays of stacking domains #1 serve as nucleation sites for controlled buckling of substrate-supported TMD bilayers under uniaxial compression.

To explore the above ideas, we develop a general framework (see section 1 in supporting information) to probe moiré pattern formation in bilayer TMDs and the structure-energy profile (Figure 2). We consider only the moiré pattern formed between the interfacial chalcogenide layers (Figure 2(a)), which carry the first-order interlayer interactions. In fact, quantum-mechanical calculations confirm that the interfacial chalcogenides dominate the interlayer interaction.<sup>42</sup> We also want to mention that the full moiré pattern

in TMD bilayers is built primarily upon such an interfacial moiré but with some additional variation (e.g., Figure 4(c)). We first consider three twist angles and three lattice mismatch strains. To construct the resulting moiré patterns (see section 1 in supporting information), two square layers of chalcogenide atoms (X and X' layers in Figure 2(a)) are first stacked together, and then an in-plane twist is applied on one layer (the bottom X' layer, shown in green). The largest lattice mismatch for heterogeneous TMD bilayers considered here is 0.03, which is consistent with computational and experimental studies in the literature.<sup>23</sup> Small twist angles are considered as they are the most relevant in our proposed approach. Further relaxation is performed using conjugate-gradient minimization on the total vdW energy of the X layer. Only out-of-plane displacements of X atoms are permitted while the bottom X' atoms are fixed (Figure 2(b)). The in-plane relaxation due to the covalent bonding present in real materials is not included here, but the out-of-plane relaxation considered here, representative of typical TMD materials, reveals the dominant physical effects of morphology engineering. The effect of in-plane relaxation is shown next in the real-material example of twisted bilayer MoS<sub>2</sub>; the results are qualitatively similar, but the area of individual domains in the moiré pattern varies.

Although there are many choices for the functional form of the vdW potential, two features are essential. First, this potential should capture the Pauli repulsion at short ranges due to overlapping electron orbitals. This is essentially the effect of steric interactions. Second, the potential should provide an attractive long-range term. Since our analysis does not concern in-plane relaxation or sliding, we choose the standard 12/6 Lennard-Jones potential to be the vdW potential in our analysis. This is sufficient to

capture the effect of steric interactions, the existence of which is universal regardless of the specific functional form of the vdW potential. In fact, it is the steric interactions that govern the height modulation among the stacking domains in a moiré, as noted below.

In this analysis of a generic TMD bilayer structure, we characterize three quantities. The first is out-of-plane relaxed vdW interaction energy, or  $E_{relaxed}$ , for each X atom, which is the sum of relaxed vdW potential  $V_{vdw}(d_{relaxed})$  of eligible pairs of interactions with the X' atom in another layer. The vdW potential used is the standard 12/6 Lennard-Jones potential (see section 1 in supporting information), where  $d_0$  is the separation at which the vdW potential reaches the minimum, same as the vertical interlayer separation between X and X' layers. In particular, for  $\epsilon_{mismatch} = 0$  and  $\theta=0$  where the alignment between X and X' atoms through out-of-plane direction is exact,  $d_{min} = d_0$  for every X atom in the unrelaxed geometry. The second is the downward height displacement  $h_{disp}$  of each X atom during the out-of-plane relaxation (Figure 2(b)). The third is the minimum interatomic distance  $d_{min}$ (Figure 2(b)), which indicates the unrelaxed distance from each X atom to its nearest neighbor in another layer.

Figure 2(c) shows the correlation between  $E_{relaxed}$ ,  $h_{disp}$ , and  $d_{min}$  of the X atomic layer for the out-of-plane-relaxed moiré patterns. Here we show three moiré patterns in the geometrical space of lattice mismatch  $\epsilon_{mismatch}$  and twist angle  $\theta$ , viewed through out-of-plane direction. The contour planes of  $E_{relaxed}$ ,  $h_{disp}$ , and  $d_{min}$  are stacked together for each moiré pattern to highlight the correlation. One can easily identify the parallelogram unit cell based on the moiré periodicity (Figure 2(c)). It is found that the unit cell vector length  $L$  decreases as  $\theta$  or  $\epsilon_{mismatch}$  increases (see section 1 in supporting information). Following the notation established in Figure 1(b), one can

identify the representative high-symmetry stacking domains (#1, #2, #3) and transitional stacking domains (#4, #5, #6). The X atoms locate on top of the X' atoms in high-symmetry stacking domains #1, while they shift to the centers of the triangles of three nearest-neighboring X' atoms in high-symmetry stacking domains #2 (or #3). They both possess hexagonal rotational symmetry. The transitional stacking domains (#4, #5, #6) are the representative transitional boundaries between high-symmetry stacking domains (#1, #2, #3). The X atoms do not sit at the symmetrical points of the triangles of X' atoms, as required by the topological transition of atomic registry symmetry from one kind of (domain #1) to another (domain #2 or #3).

The energy and height (interlayer spacing) profile of all six representative stack domains satisfies the condition described in Figure 1(c). For example, stacking domains #2 and #3 have the lowest energy and smallest interlayer spacing. The stacking domains #1 are responsible for the “puddles” on the contour planes of  $d_{min}$ . In addition, the location where  $d_{min}$  is larger corresponds to the location where  $|h_{disp}|$  is larger, indicating strong presence of steric interactions between chalcogenide atoms at the interface during relaxation. As a result, the #1 stacking domains are responsible for the “bumps” on the contour planes of  $-|h_{disp}|$ , which are correlated to the interlayer separation profile (height). As a natural consequence of larger interlayer separation in a vdW system, the #1 stacking domains are responsible for the “bumps” on the contour planes of  $E_{relaxed}$ . As a result, a periodical array of morphological perturbations with larger interlayer spacing and higher energy emerge in the bilayer. These perturbations are the #1 stacking domains. Coincident with the moiré periodicity of the bilayer, such perturbations are crucial for morphology engineering of substrate-supported TMD bilayers when an in-plane

compression is applied: these #1 stacking domains are the preferred buckling initiation sites.

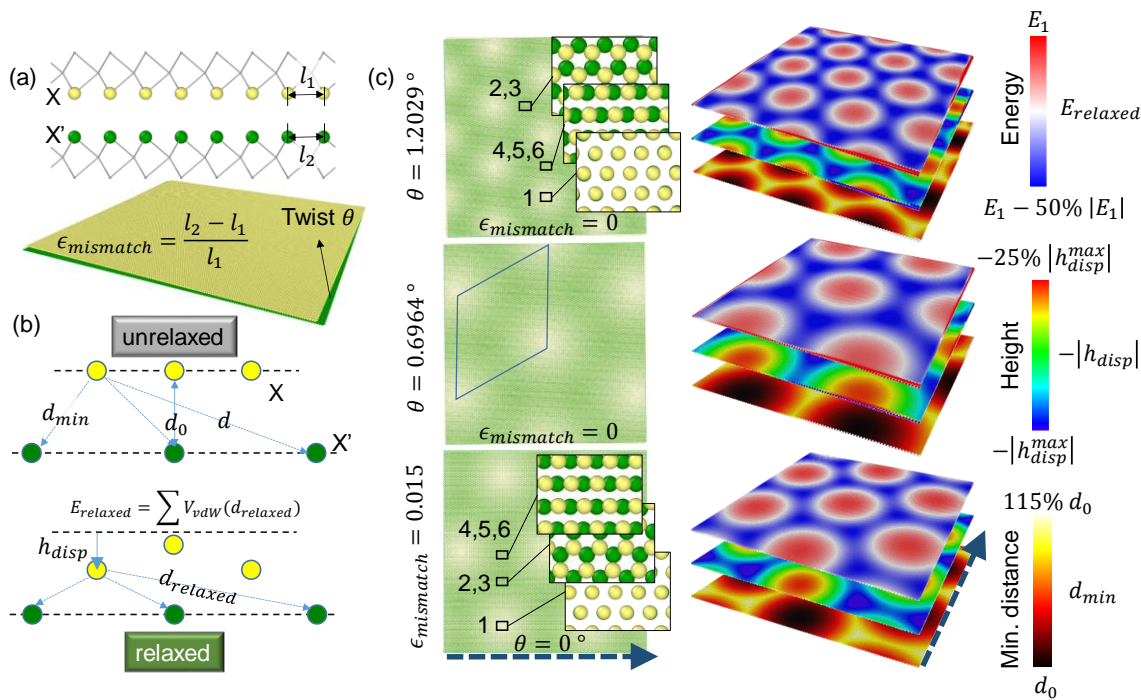


Figure 2: (a) Using the interfacial chalcogenide layers to probe the moiré pattern of bilayer TMDs. Two square layers of chalcogenide atoms (X (yellow) and X' (green) layers) are first stacked and then an in-plane twist is applied on one layer. The twist angle can be zero. Lattice mismatch strains are also considered, as is common in heterogeneous bilayers. (b) Relaxed vdW interaction energy  $E_{relaxed}$ , downward height displacement  $h_{disp}$  after relaxation, and minimum interatomic distance  $d_{min}$  indicating the unrelaxed distance from each X atom to its nearest neighbor in X' layer. The relaxation only allows out-of-plane displacement while keeping X' atoms fixed.  $d_0$  is the interatomic distance  $d$  at which the vdW potential reaches the minimum. (c) Correlation between  $E_{relaxed}$ ,  $-|h_{disp}|$  and  $d_{min}$  of the X atomic layer in the moiré pattern. The contour planes of  $E_{relaxed}$  (top),  $-|h_{disp}|$  (middle) and  $d_{min}$  (bottom) are stacked together for comparison. It is found that locations where  $d_{min}$  is larger correspond to locations where  $|h_{disp}|$  is larger, indicating a strong presence of steric interactions between chalcogenide atoms at the interface during relaxation. The #1 stacking domains are responsible for the “bumps” on the contour planes of  $-|h_{disp}|$  and  $E_{relaxed}$ . When an in-plane compression is applied, #1 stacking domains are the preferred buckling initiation sites. Quantified numbers in this calculation:  $E_1 = -3$  eV,  $|h_{disp}^{max}| = 0.06$  nm,  $d_0 = 0.339$  nm. The interatomic spacing in the X layer is 0.319 nm. The dashed arrows mark the orientation of the layers in the contour planes to guide the comparison with the moiré patterns.

Next, without losing generality, we use twisted bilayer MoS<sub>2</sub> to further clarify our approach. We use continuum mechanics (CM) modeling, molecular dynamics (MD)

simulation, and density functional theory (DFT) calculation to demonstrate this mechanics-based materials programming approach. MD simulation of MoS<sub>2</sub> is carried out in LAMMPS<sup>43</sup> using the ReaxFF reactive force field,<sup>44</sup> which is based on quantum mechanical simulations and is expected to provide the best accuracy. MD simulation is used to calculate the deformation with atomic resolution while the CM modeling is used to establish a mechanics basis for the design approach. Finally, DFT calculations, carried out in SIESTA,<sup>45</sup> are used to demonstrate the applications in designing electronic and optical properties of multilayer TMDs.

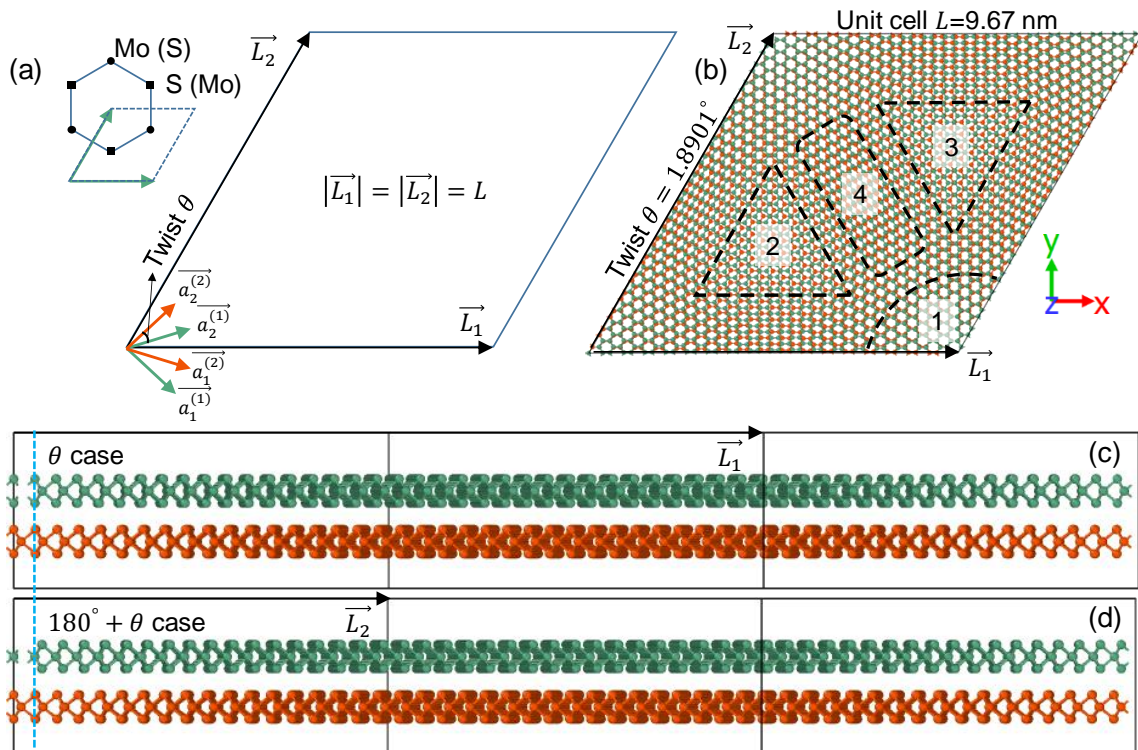


Figure 3: (a) Unit cell structure in commensurate twisted stacking of bilayer MoS<sub>2</sub>. This is a simplified version of the more general version as in Figure 1. There are two in-plane sublattice sites to put Mo and S alternatively. (b) The top view (z-view) of a unit cell lattice (without relaxation) with a small twist angle. Regions indicated by dashed boxes represent the precursors (i.e., without relaxation) of stacking domains, labeled in the same way as Figure 1(b). Upon relaxation (see Figure 4), these regions further evolve to minimize energy. (c) and (d): The side view (y-view) of two types of twisted bilayer MoS<sub>2</sub> ( $\theta$  case and  $180^\circ + \theta$  case), caused by the

swap of pattern of Mo and S on the in-plane sublattice sites of one layer (e.g., contrast highlighted by dashed blue line, and also the periodical box boundary).

Figure 3(a) shows the unit cell structure in commensurate twisted stacking of bilayer  $\text{MoS}_2$  (see section 2 in supporting information), as a specific material example from the generic description in Figure 1(a). In accordance with the ReaxFF force field to be used in later MD simulations, the length of the lattice vector (e.g.,  $\overline{a_1^{(1)}}$ ) is 0.319 nm.<sup>44</sup> In the hexagonal lattice of each layer, there are two in-plane sublattice sites, and there are two choices of where to position alternatively the single Mo atom and the pair of two S atoms on these sites (Figure 3(a)). Because of this, there are two co-existing types of twist cases (Figure 3(c)), termed  $\theta$  case and  $180^\circ + \theta$  case. These two cases differ by the pattern of Mo and S on the in-plane sublattice sites of one layer, while that of the other layer remains unchanged. Figure 3(b) shows the out-of-plane view (z-view) of an exemplary unit cell lattice with a twist angle of  $1.8901^\circ$ . The construction here is purely geometrical and relaxation is not performed yet. Following the discussion and notation in Figure 1(b), we are able to identify the initial formation of periodical stacking domains, before relaxation.

Figure 4(a) shows the twisted moiré pattern in the  $\theta$  case for bilayer  $\text{MoS}_2$  supported on a substrate after relaxation (see section 3 and 4 in supporting information) for three decreasing twist angles (increasing unit cell size). Stacking domain regions are labeled in the same way as in Figure 1(b). We then examine the detailed stacking domains for these regions for both the  $\theta$  case (Figure 4(c)) and the  $180^\circ + \theta$  case (Figure 4(d)). Following the conventional notation of high-symmetry stacking in bilayer  $\text{MoS}_2$ ,<sup>46</sup> we find that for the  $\theta$  case, circle-shaped domain #1 has AA stacking, while the triangle-shaped domains

#2 and #3 both have 3R stacking. Although domains #2 and #3 have identical stacking, they appear different because 3R stacking lacks inversion symmetry and domain #2 is the inverted version of domain #3 (Figure 4(c)). Here we want to emphasize the finding that twisted bilayer MoS<sub>2</sub>, with the moiré pattern, is able to create large scale periodical arrays of 3R stacking, which carry potential significance for the application of 3R-stacked MoS<sub>2</sub> in optoelectronic valleytronics,<sup>12, 13, 47, 48</sup> where the presence of inversion asymmetry is essential. For the  $180^\circ + \theta$  case, the circle-shaped domain #1 has A'B stacking, while the triangle-shaped domains #2 and #3 have AB' and 2H stacking, respectively. Compared with the unrelaxed configurations of the same unit cell size (e.g., twist  $\theta = 1.8901^\circ$  in Figure 4(a) and Figure 3(b)), the areas of stacking domains #2 and #3 (3R, AB' and 2H) increase, while those of stacking domain #1 and #4 (AA and A'B) decrease. The areas of regions #2 and #3 are larger than those of regions #1 and #4, and such contrast increases with the decrease in twist angle (or increase in unit cell size), since the area of region #1 remains roughly unchanged. Such changes of area occur during relaxation, which suggests that energies of the shrinking domains (#1 and #4, AA and A'B) are higher than those of the expanding domains (#2 and #3, 3R, AB' and 2H). This is to be verified in Figure 5. The change of domain #4 is coupled with that of domain #2 (#3) since domain #4 is essentially the boundary between domain #2 and #3. The same trends can be found in the  $180^\circ + \theta$  case (Figure 4(b)).

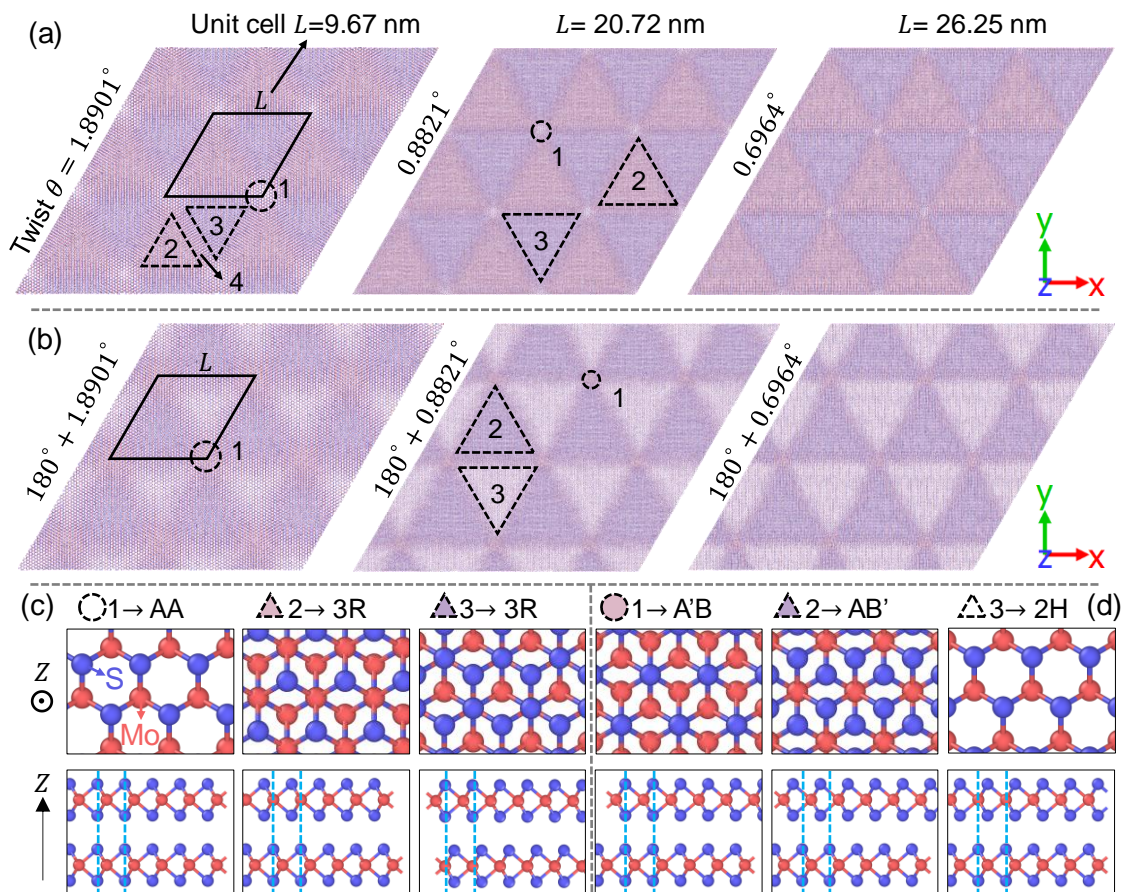


Figure 4: (a) From left to right are three examples of the twist  $\theta$  case with increasing unit cell size after relaxation. For clarity, we show a supercell consisting of 9 unit cells (3x3). The color code for atoms is shown in (c). The area of stacking domains #2 and #3 increase on relaxation, while the area of stacking domain #1 remains roughly unchanged. The change of domain #4 is coupled to that of domains #2 and #3 since domain #4 is essentially the boundary between domains #2 and #3. (b) Same as (a) but for twist  $180^\circ + \theta$  case. (c) and (d): Detailed structure of the stacking domains for twist  $\theta$  case (as in (a)) and  $180^\circ + \theta$  case (as in (b)), respectively. The top and bottom rows have orthogonal viewing perspectives. The blue dashed line is a visual guide to identify the stacking arrangements of the atoms.

Figure 5 validates the proposed coupling of stacking energy and morphological perturbation in substrate-supported twisted bilayer MoS<sub>2</sub> with the moiré pattern. Figure 5(a) shows the construction of a rectangular unit cell (indicated by the box) for each stacking pattern. These unit cells are used in atomistic simulations to study (see section 5 in supporting information) interlayer distance (Figure 5(b)), total energy (Figure 5(c)), and in-plane mechanical stiffness (Figure 5(d)), in the presence of a substrate. The trend

shown in Figure 5(b) and Figure 5(c) among the five stacking patterns shows that AA and A'B stacking have the largest interlayer distance and highest total energy. Close inspection of the vertical alignment (out-of-plane direction) of the S atoms at the interface (e.g., the dashed blue circles in Figure 5(a) and the dashed line in Figure 4(c)) shows that the steric interaction between interfacial S atoms is strongly correlated to the interlayer distance, consistent with early predictions in Figure 2. The calculated trend from Reaxff force field simulation agrees with literature reported DFT calculations.<sup>46</sup> We note that due to the existence of the substrate interaction potential in our simulation, the interlayer distance and the total energy are reduced relative to the substrate-free cases from DFT calculations.<sup>46</sup> Figure 5(d) shows the biaxial stress-strain curves for each stacking pattern, modeled in the rectangular unit cell as shown in Figure 5(a), under equibiaxial compression up to 10%. We can see that the largest-separation stacking, AA and A'B, are the most mechanically compliant, as their stresses are lower than other stacking patterns. This confirms that largest-separation stacking patterns, AA and A'B, have the weakest interlayer mechanical coupling. Lastly, Figure 5(e) shows the morphological variation of the top layer of moiré-twisted bilayer MoS<sub>2</sub> on a substrate, for two  $\theta$  cases and two  $180^\circ + \theta$  cases. For visual clarity, the topmost S layer is colored according to the height variation within this S layer. One can immediately see that twist-moiré bilayer MoS<sub>2</sub> naturally possesses a periodical array of morphological perturbations, consisting of higher-energy and larger-interlayer-separation stacking domains #1, connected by stacking domains #4, in agreement with the prediction in Figure 1(b). With the largest interlayer separation and the lowest mechanical stiffness, AA and A'B stacking domains are the preferred buckling initiation sites for moiré-twisted bilayer MoS<sub>2</sub> if in-plane

compression is applied. The spacing between these preferred buckling initiation sites is precise and protected by the periodicity of the moiré superlattice. Therefore, the buckling deformation has the potential to be programmed.

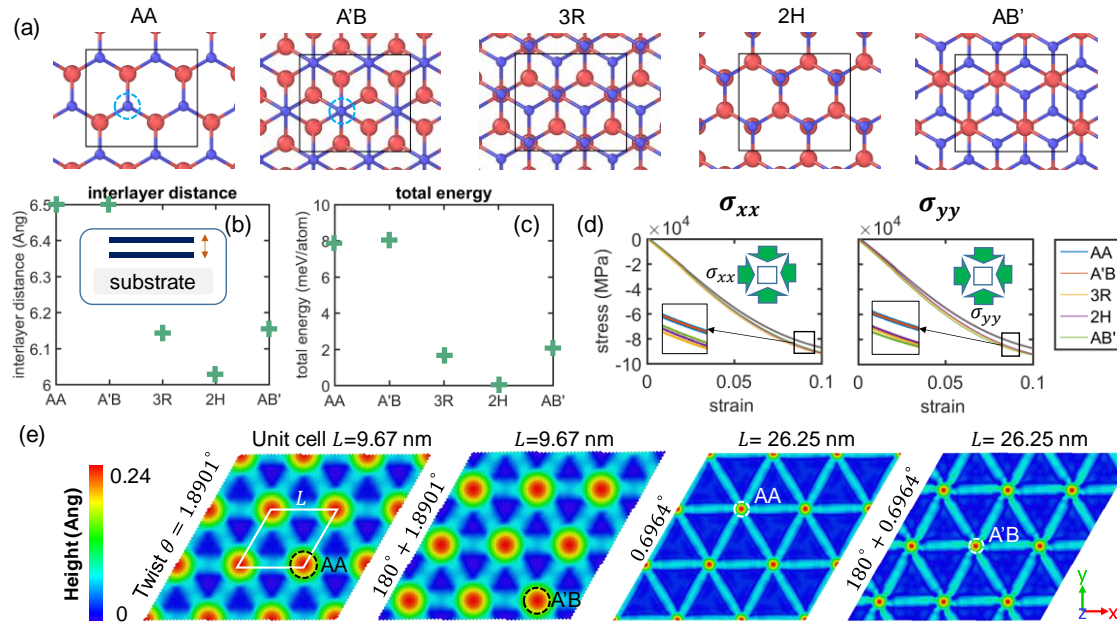


Figure 5: (a) Atomistic structure of five high-symmetry stacking arrangements. The rectangular boxes denote unit cells for each stacking pattern to be used in characterization of interlayer distance as in (b), total energy as in (c), and in-plane mechanical stiffness as in (d), as the bilayer is supported on a substrate. Dashed blue circles highlight the vertical alignment of the S atoms. (b) and (c) show that AA and A'B stacking have the largest interlayer distance and highest total energy. (d) The comparison of biaxial stress-strain curves of all stacking patterns under biaxial compression, which indicates that AA and A'B stacking have the lowest in-plane mechanical stiffness. (e) The height variation of the top S layer of the top layer of moiré-twisted bilayer MoS<sub>2</sub> on a substrate. The white box denotes the unit cell. It shows that AA and A'B stacking domains are the preferred buckling initiation sites under in-plane compression. The spacing between these preferred buckling initiation sites is precise and protected by moiré symmetry.

Illustrating the proposed mechanism, Figure 6 shows the programmable morphology engineering based on the buckling pattern and feature spacing of twisted bilayer MoS<sub>2</sub>, activated by a global in-plane compression, using just one twist angle as an example. In an experiment, such a global compression would typically be introduced by the relaxation of a pre-stretched flexible substrate (e.g., Figure 1(d)).<sup>6</sup> The deformed morphologies of

the twisted bilayer are colored by height. The relation between the orientation of buckling initiation sites (examined in Figure 5) and compression directions (X and Y) are shown at the schematic on the top left of Figure 6. In the case of a uniaxial compression along the Y direction (leftmost column in Figure 6), as the applied compression  $\epsilon_{yy}$  increases, the buckling initiation sites initiate the local buckling, forming isolated periodical bubbles. At small  $\epsilon_{yy}$ , the shape of the bubble looks rather circular. Increasing  $\epsilon_{yy}$  causes anisotropy in the shape of the bubble. The bubble starts to elongate less long the Y direction, and more along the X direction. Beyond a certain compression level, the bubbles connect along the X direction, forming wrinkles. As a result, a periodical array of wrinkles, equally spaced along the Y direction, is obtained. More importantly, the feature spacing between these wrinkles  $L_s(\epsilon_{yy})$  can be precisely controlled by the applied global compression  $\epsilon_{yy}$  and the moiré unit cell size  $L(\theta)$ , from the simple geometrical argument shown schematically in the inset to Figure 6.

In the case of a uniaxial compression along the X direction (bottom row in Figure 6), the process is very much similar to that of Y direction. The major difference is that the bubbles can not connect in the Y direction at the same maximum applied compression (10%). This is understandable since the smallest projected distance between the buckling initiation sites along the Y direction is much larger than that along the X direction. As a result, the Y-elongated bubbles remain isolated. Again, the feature spacing between these isolated bubbles  $L_s(\epsilon_{xx})$  can be precisely controlled by the applied global compression  $\epsilon_{xx}$  and the moiré unit cell size  $L(\theta)$ , shown schematically in Figure 6.

In the case of an equi-biaxial compression (along the diagonal in Figure 6), at small biaxial strain, the shape of the bubble looks rather circular. Increasing the biaxial strain

causes anisotropy in the shape of the bubble. Unlike uniaxial compression, the bubbles begin to adopt a triangular shape and form a triangular array. Similarly, the feature spacing between these triangular bubbles  $L_s(\epsilon_{xx} = \epsilon_{yy})$  can be precisely programmed by the applied global biaxial compression  $\epsilon_{xx} = \epsilon_{yy}$  and the moiré unit cell size  $L(\theta)$ .

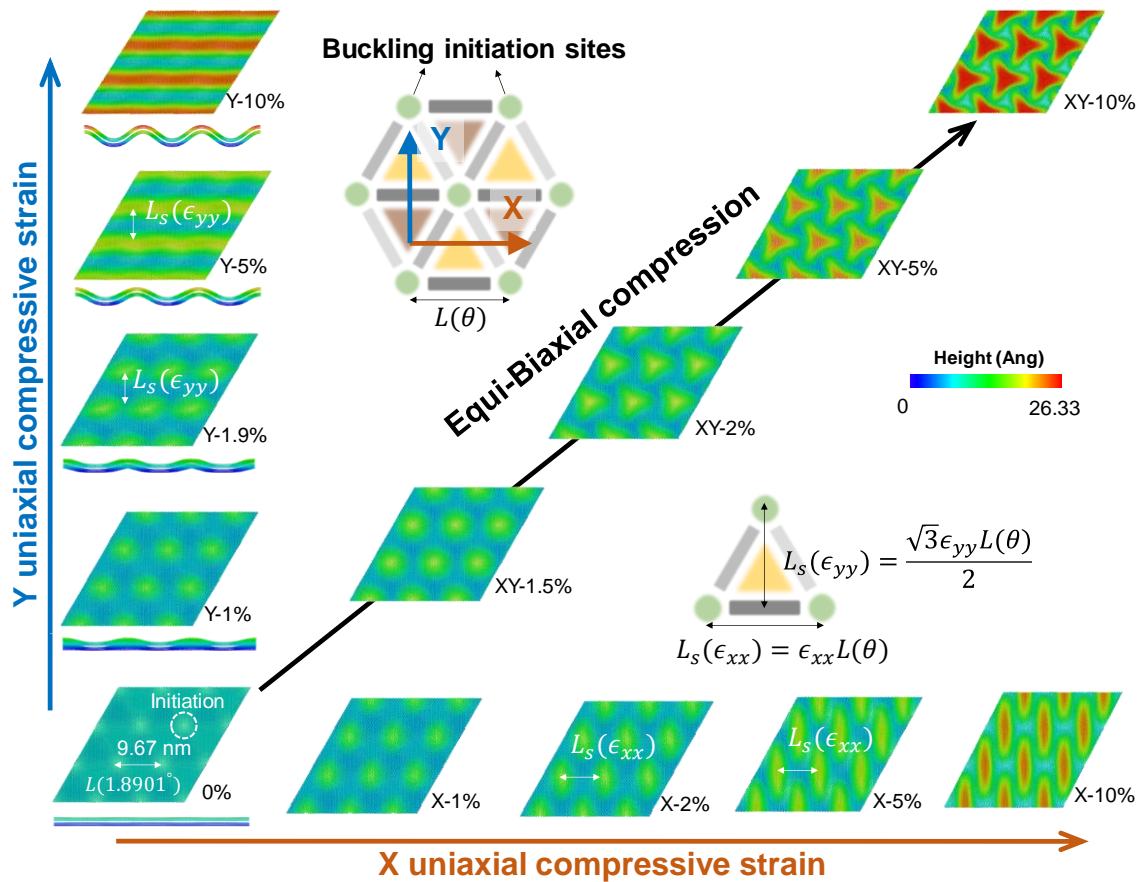


Figure 6: Moiré-templated programmable morphology engineering, using the twist  $\theta = 1.8901^\circ$  case as an example. Morphological evolution snapshots from MD simulations are colored by height. The X and Y directions, and the orientation of buckling initiation sites are shown schematically in the inset. The maximum applied compression is 10 % in either X or Y direction. The buckling initiation sites initiate the local buckling, immediately forming isolated periodical bubbles. Y uniaxial compression results in a periodical array of wrinkles, equally spaced along Y direction, where side views in the X direction are provided at the bottom of each snapshot. X uniaxial compression results in a triangular array of isolated Y-elongated bubbles. Equi-biaxial compression results in a triangular array of triangular bubbles. The feature spacing  $L_s(\epsilon_{xx}, \epsilon_{yy})$

in all these patterns can be precisely programmed by the applied compression ( $\epsilon_{xx}$ ,  $\epsilon_{yy}$ ) and the moiré unit cell size ( $L(\theta)$ ), from the geometric construction shown schematically.

The key feature of the proposed morphology engineering approach is the precise control of the featured shape type (e.g., wrinkles) and feature spacing (as shown in Figure 6). These are protected by the intrinsic periodicity of the moiré superlattice and the in-plane anisotropy in the mechanics and energetics of the stacking domains. With the feature spacing precisely determined from the given compression and the moiré superlattice, one can further design the spatial profile and the strain distribution within the feature, providing additional control over electronic structure and optical properties.

We now consider a continuum mechanics representation of programmable wrinkle formation to facilitate design. We seek an approximate solution within the applied strain range. Besides the feature spacing  $L_s$ , two other characteristic morphological quantities, as shown in Figure 7(a), are delamination length  $L_d$ , and amplitude  $A$ . They are expected to depend upon the moiré-twist angle  $\theta$  and the applied strain  $\epsilon_{yy}$ . The weak interlayer vdW interaction in the twisted bilayer MoS<sub>2</sub> allows the deformation of one layer to be more weakly coupled to that of the other layer via interfacial sliding. This is evident in Figure 7(b), where the proximity of a pair of S atoms, residing on different layers, is traced during increasing Y compression. Given the decoupled nature of deformation of the bilayer, the large deformation can be modeled more simply by only explicitly considering the bottom layer. If the spatial profile of the wrinkled bottom layer is obtained, the top layer can be assumed to conform to the bottom layer with the appropriate interlayer separation. Other explicitly considered material parameters are the bending stiffness<sup>44, 49</sup> and the in-plane stiffness<sup>44</sup> of monolayer MoS<sub>2</sub>, and substrate adhesion (see section 6 in supporting information for details). The interlayer adhesion

energy can be calculated as the interfacial energy density multiplied by the interfacial area. During post-buckling deformation, the change of interlayer adhesion energy is assumed to be small because due to the conformity of the top layer to the bottom layer, the change of interlayer adhesion energy and the interfacial area is small. Therefore, the interlayer adhesion energy is not included in our continuum mechanics model.

The coupling of the surface strain  $\epsilon_s$  and the neutral layer strain  $\epsilon_n$  to the first-order and second-order derivatives (e.g., slope, radius of curvature) of the wrinkle profile can be obtained from a mechanics analysis. As shown in Figure 7(c), the surface strain  $\epsilon_s$  (e.g., concerning the interatomic spacing in the layer of S atoms in  $\text{MoS}_2$ ) is determined by the sum of neutral layer strain  $\epsilon_n$  and the bending induced strain,  $\pm t/2R$ , where  $R$  is the radius of curvature,  $t$  is the separation of the two surfaces, and the sign depends on the side of the bent region under consideration. The neutral layer strain  $\epsilon_n$  varies across the wrinkle profile. Its gradient is closely related to the change of slope of the wrinkle profile. In the current morphology engineering approach, the neutral layer sustains compressive strain across the wrinkle profile in order to balance the global compression that initiates the buckling. The spatial profile of the wrinkled bottom layer is obtained by numerically minimizing the total energy, which is a numerical integration of bending strain energy, normal strain energy, and substrate adhesion energy along the wrinkle profile.

To put the merit of mechanics design in perspective, if the mechanical properties of the TMD layer and substrate adhesion strength are known, then the spatial profile of the wrinkle can be designed from moiré-twist angle  $\theta$  and applied strain  $\epsilon_{yy}$  (Figure 7(c)). To make this point, we apply the CM model to wrinkle formation in three cases of twist angle, and compare the results to those from the atomistic simulation. For the purpose of

obtaining a simplified approximate solution, we assume the shape of the wrinkled part to be a Gaussian. We are interested in the post-buckling range since that is where the wrinkle forms. Figure 7(d) shows that reasonable agreement is obtained among the dimensionless amplitude  $A/L_s$  and delamination length  $L_d/L_s$  of the post-buckled range for both atomistic and continuum models, indicating that the mechanics design framework has captured the dominant physics of the problem, which allows the development of other possible mechanics design approaches with varying degrees of accuracy. The comparison also shows that the spatial profile of the wrinkle is almost insensitive to whether it is the  $\theta$  case or the  $\theta + 180^\circ$  case. This is understandable since the feature spacing  $L_s$  is the same for both the  $\theta$  and  $\theta + 180^\circ$  cases, and the deformation of the bilayer is decoupled.

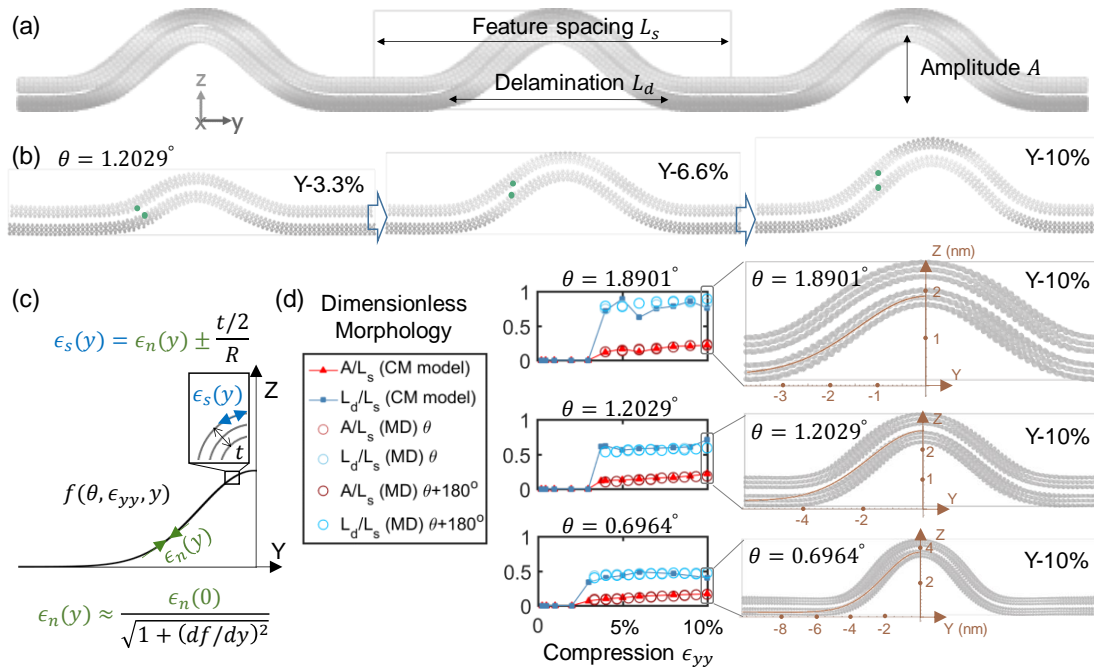


Figure 7: (a) Three characteristic morphological quantities of the wrinkled bilayer: feature spacing  $L_s$ , delamination length  $L_d$ , and amplitude  $A$ . (b) Decoupled nature of the wrinkling process of the moiré-twisted bilayer  $\text{MoS}_2$  in the post-buckling stage. The green dot marks a pair of S atoms on opposite layers. Their relative position changes, indicating sliding between the layers. The decoupled nature permits a simplified treatment using a continuum mechanics (CM) model.

model that explicitly considers only the bottom layer. If the spatial profile of the wrinkled bottom layer is obtained, the profile of the top layer is the same as that of the bottom layer with the proper interlayer separation. (c) The spatial profile of the wrinkle is a function of the moiré-twist angle  $\theta$ , applied strain  $\epsilon_{yy}$ , and Y coordinate. The surface strain  $\epsilon_s$  and neutral layer strain  $\epsilon_n$  are related to the radius of curvature  $R$  and the first-order derivative of the profile. (d) With the feature spacing  $L_s$  precisely controlled, the delamination  $L_d$  and amplitude  $A$  can also be predicted from continuum mechanics (CM) modeling. Here the comparison of dimensionless wrinkled morphology calculated from the CM model and the atomistic model shows reasonably good agreement. We are interested in the post-buckling range since that is where the wrinkle forms. The spatial profile of the wrinkle is almost insensitive to whether it is  $\theta$  case or the  $\theta + 180^\circ$  case. The rightmost column shows an example comparing the spatial profiles of both the CM model and the atomistic model at 10 % Y compression.

Finally, with the morphology engineering approach, we can envision a wide range of emerging opportunities for optoelectronic applications. Figure 8(a) depicts a possible device setup, where a morphology and strain engineered TMD bilayer with a moiré pattern serves as the base functional layer on a flexible substrate. More TMD layers can be transferred on top, and will conform to the morphological features beneath. In other words, with this approach it should be possible to achieve vdW multilayered structures of TMDs with prescribed morphology. In the context of a morphology-strain-engineered vdW heterostructure of TMDs with type-II band alignments<sup>16, 20-26</sup> where each TMD monolayer maintains its own band structure,<sup>16-18</sup> the overall optical absorption is expected to come from the properties of each individual morphology-strain-engineered TMD monolayer,<sup>19</sup> with the relative position of the band edges among different TMDs subjected to change from morphology-strain engineering.<sup>2, 50, 51</sup> Therefore, there is a huge variety of structure-property relationships yet to be explored, with the morphology-strain-engineered TMD monolayer as the fundamental functional building block. Considering that the wrinkled moiré bilayer has very large moiré periodicity and wrinkle spacing, first-principles calculations of such a large bilayer system are known to be computational prohibitive. To show the first-order picture, here we take the monolayer MoS<sub>2</sub> as an

example to illustrate the prospect of morphology-strain-engineered electronic and optical properties in a TMD monolayer; recent first-principles computational studies and experimental investigations have confirmed the primary role of the monolayer structure.<sup>16-26</sup> Nevertheless future computational efforts are required to fully explore bilayer and multilayer structure in the context of morphology-strain engineering. We believe that understanding such a monolayer is the first step towards the full understanding of morphology-strain-engineered bilayer or multilayer structure. We employ DFT calculations for the related investigation (see section 7 in supporting information). The generalized gradient approximation (GGA) in the framework of Perdew-Burke-Ernzerhof (PBE) is adopted for the exchange-correlation potential. Numerical atomic orbitals with double zeta plus polarization are used for the basis set. Next we illustrate at least two tunable quantities.

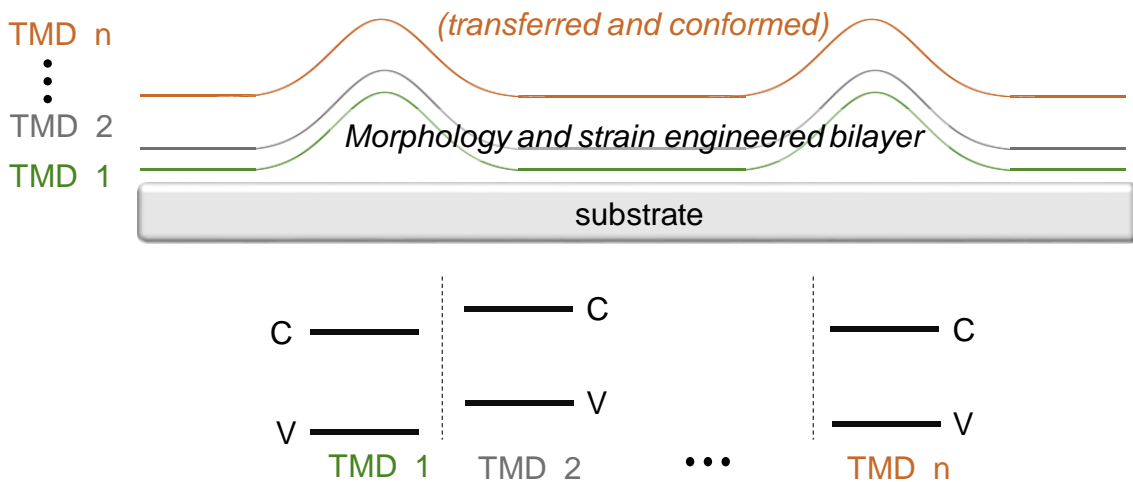


Figure 8: Envisioned morphology and strain engineered vdW heterostructure of TMDs with type-II band alignments. The base feature on a substrate is the morphology and strain engineered heterobilayer with moiré pattern. More heterolayers of TMDs can then be transferred on top and they are expected to conform to the engineered morphology feature underneath. The overall optical absorption of such a structure is expected to depend on independent contributions from each morphology-strain-engineered TMD monolayer, and the relative positions of the band edges among different TMDs are subjected to change from morphology-strain-engineering.

The first is the nanoscale curvature-induced modulation of local band gaps. Our DFT calculation on the projected density of states (PDOS) shows that the local electronic band gap is strongly correlated to the local spatial curvature (Figure 9). Larger local curvature corresponds to smaller local band gap. Such a spatial variation of band gap can contribute to a funneling effect on the excited electron-hole pairs.<sup>1,6</sup>

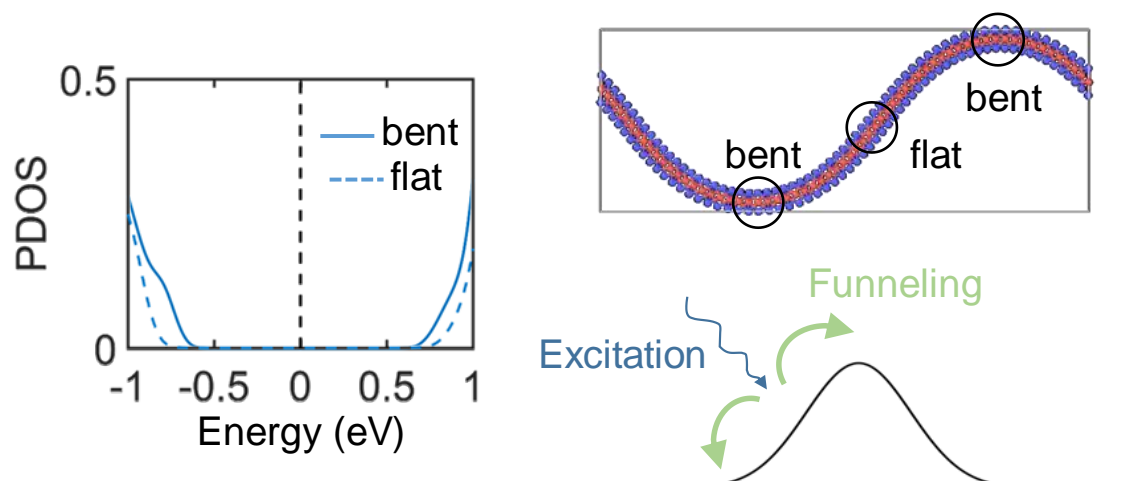


Figure 9: Demonstration of the effect of local curvature of an MoS<sub>2</sub> monolayer on the projected density of states and band gaps, which is important for exciton funneling. Larger local curvature corresponds to a smaller gap.

The second is the global morphology-induced modulation of optical absorption. Our DFT calculation on the optical absorption spectra of the wrinkled MoS<sub>2</sub> monolayer shows a strong morphology dependence (Figure 10). We consider two orthogonal polarization directions for the incident light. We find that the absorption spectrum for each polarization can be tuned via morphology control, and that there are two representative morphology-dependent absorption peaks. For polarization #1 where the polarization direction is parallel with the substrate, all three morphologies exhibit peak #1 (near 2.5 eV), while the most wrinkled morphology #3 has the largest reduction in peak #1

intensity and the largest increase in peak #2 intensity. For polarization #2 where the polarization direction is perpendicular to the substrate, all three morphologies exhibit peak #2 (near 5 eV), while the most wrinkled morphology #3 has the largest reduction in peak #1 intensity and the largest increase in peak #2 intensity. Furthermore, the strongest intensity of peak #1 stems from the polarization that is parallel to all of the monolayer, while the strongest intensity of peak #2 stems from the polarization that is perpendicular to all of the monolayer. These two standard cases can be found in the flat morphology. Nevertheless, for a wrinkled morphology, some portions of the monolayer are neither parallel with nor perpendicular to a polarization direction, and therefore the absorption of these portions behaves as a mixture of the two standard cases. As a result, in the absorption spectrum for an evolving wrinkled morphology for one polarization, one finds increased absorption intensity near an energy range that is the typical absorption peak energy range in another polarization direction (e.g., peak #1 in the absorption spectrum of polarization #2), as the degree of wrinkling increases.

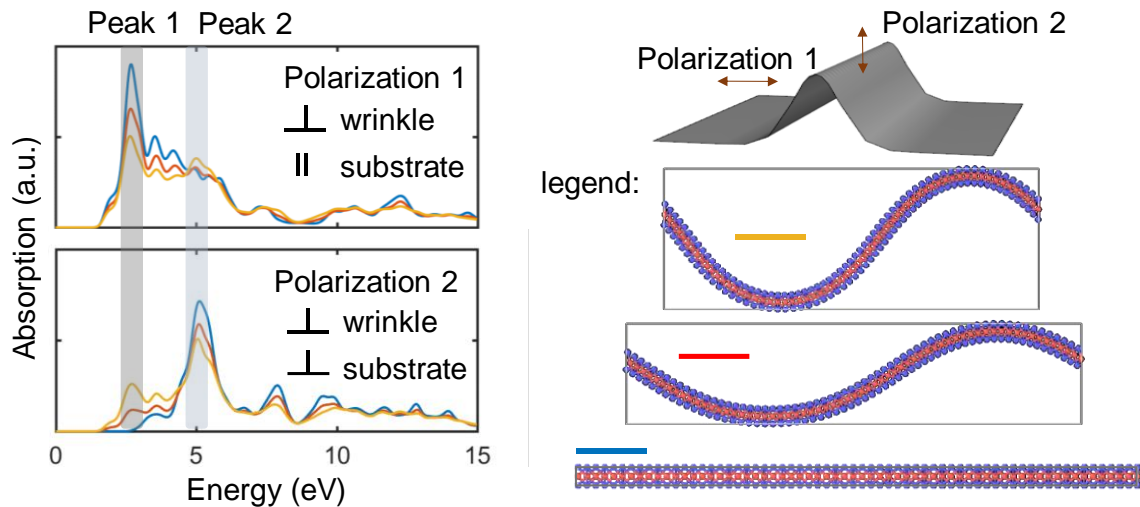


Figure 10: Morphology-dependent optical absorption of an MoS<sub>2</sub> monolayer for incident light in two orthogonal polarization directions. Peaks 1 and 2 are two representative morphology-dependent absorption peaks.

In the context of the current proposed morphology engineering approach, the lattice strain and bending curvature of each TMD monolayer can be programmed. The above analyses of morphology-strain-engineered band gap and optical absorption of a TMD monolayer clearly indicate emerging possibilities for programmable design of a rich spectrum of structure-property relationships in multilayer TMDs.

### **3. Conclusions**

In conclusion, we have proposed a general moiré-templated nanoscale morphology engineering approach applicable to bilayer and multilayer TMDs. The moiré superlattice plays a central role in generating in-plane anisotropy in both morphological interlayer spacing and mechanical stiffness of periodical stacking domains. Upon global in-plane compression, high-energy, large-interlayer-separation periodic commensurability domains, a consequence of the moiré pattern, serve as buckling initiation sites. During the post-buckling stage, the spacing between the buckled features can be precisely correlated to the moiré periodicity and the applied compressive strain. With the feature spacing known, the spatial profile of the morphology and strain profile can be pre-determined, providing a bridge to electronics and optics design. We take twisted bilayer MoS<sub>2</sub> as an example to implement our morphology engineering approach. We further demonstrate how the morphology can modulate band gap and optical absorption of an MoS<sub>2</sub> monolayer, envisioned as a constituent layer of a morphology-strain engineered vdW TMD heterostructure, enabled by the current approach. A rich spectrum of structure-property relationships of morphology-strain engineered multilayer TMDs has yet to be explored and calls for further computational and experimental effort.

#### 4. Methods

*DFT calculation:* We take the structure snapshot at several deformations from MD simulation as input for DFT calculation. Slab model is used to ensure enough vacuum space in the out-of-plane direction. The generalized gradient approximation (GGA) in the framework of Perdew-Burke-Ernzerhof (PBE) is adopted for the exchange-correlation potential. Numerical atomic orbitals with double zeta plus polarization are used for the basis set, with a plane-wave energy cutoff of 500 Ry. Geometric structures are relaxed until the force on each atom is less than  $0.01 \text{ eV \AA}^{-1}$  and the convergence criteria for energy is  $10^{-5} \text{ eV}$ . For optical absorption calculation (the imaginary part of dielectric function), five times denser K-points were used and self-consistent field tolerance is  $10^{-6}$ . The electronic smearing temperature during all calculations is 300 K. See supporting information for more details.

*MD simulation:* The substrate effect is modeled using a virtual wall. Before deformation, energy minimization is performed. The deformations for X, Y and equi-biaxial is carried in a quasi-static mode. After each incremental time step, energy minimization is performed. See supporting information for more details.

*Continuum mechanics modeling:* First we assuming the profile of the wrinkle. Then we calculate the associated bending energy, substrate adhesion energy, and the membrane compression strain energy. Finally we minimizing the total energy (summation of the above energies) to quantify the profile of the wrinkle. See supporting information for more details.

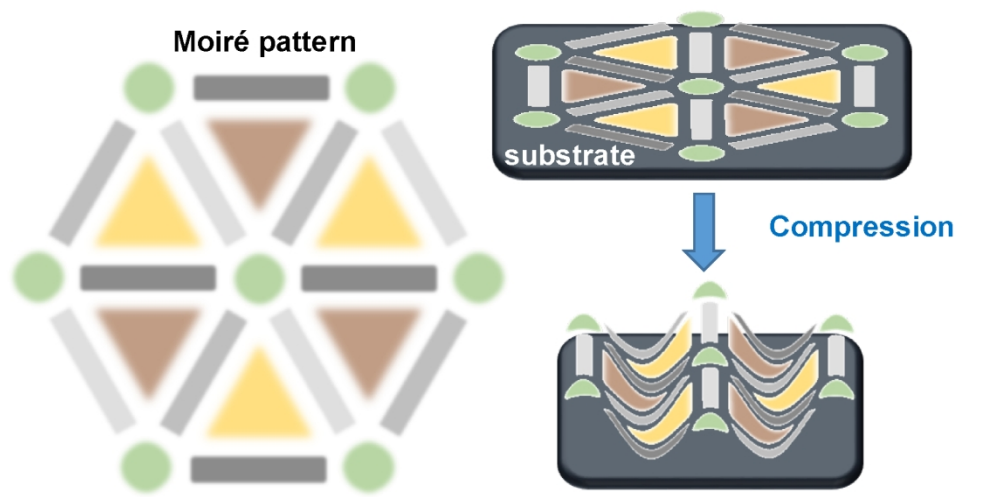
**Conflicts of interest:** The authors declare no conflict of interest.

**Acknowledgement:** We thank financial support from Army Research Office grant W911NF-17-1-0544 and UIUC-ZJU joint institute. We also acknowledge helpful discussion with Dr. Pascal Pochet.

### References:

1. J. Feng, X. Qian, C. Huang and J. Li, *Nature Photonics*, 2012, **6**, 865-871.
2. H. Conley, B. Wang, J. Ziegler, R. Haglund, S. Pantelides and K. Bolotin, *Nano Letters*, 2013, **13**, 3626-3630.
3. K. He, C. Poole, K. Mak and J. Shan, *Nano Letters*, 2013, **13**, 2931-2936.
4. H. Li, A. Contryman, X. Qian, S. Ardakani, Y. Gong, X. Wang, J. Weisse, C. Lee, J. Zhao, P. Ajayan, J. Li, H. Manoharan and X. Zheng, *Nature Communications*, 2015, **6**, 7381.
5. J. HULTEEN and R. VANDUYNE, *Journal of Vacuum Science & Technology a-Vacuum Surfaces and Films*, 1995, **13**, 1553-1558.
6. A. Castellanos-Gomez, R. Roldan, E. Cappelluti, M. Buscema, F. Guinea, H. van der Zant and G. Steele, *Nano Letters*, 2013, **13**, 5361-5366.
7. K. Novoselov, A. Mishchenko, A. Carvalho and A. Neto, *Science*, 2016, **353**, aac9439.
8. S. Tan, Z. Sofer, J. Luxa and M. Pumera, *Acs Catalysis*, 2016, **6**, 4594-4607.
9. J. Luxa, P. Vosecky, V. Mazanek, D. Sedmidubsky, M. Pumera and Z. Sofer, *Acs Catalysis*, 2018, **8**, 2774-2781.
10. J. Luxa, O. Jankovsky, D. Sedmidubsky, R. Medlin, M. Marysko, M. Pumera and Z. Sofer, *Nanoscale*, 2016, **8**, 1960-1967.
11. A. Geim and I. Grigorieva, *Nature*, 2013, **499**, 419-425.
12. W. Yao, D. Xiao and Q. Niu, *Physical Review B*, 2008, **77**, 235406.
13. D. Xiao, G. Liu, W. Feng, X. Xu and W. Yao, *Physical Review Letters*, 2012, **108**, 196802.
14. S. Wu, J. Ross, G. Liu, G. Aivazian, A. Jones, Z. Fei, W. Zhu, D. Xiao, W. Yao, D. Cobden and X. Xu, *Nature Physics*, 2013, **9**, 149-153.
15. P. Koskinen, I. Fampiou and A. Ramasubramaniam, *Physical Review Letters*, 2014, **112**, 186802.
16. K. Kosmider and J. Fernandez-Rossier, *Physical Review B*, 2013, **87**, 075451.
17. H. Komsa and A. Krasheninnikov, *Physical Review B*, 2013, **88**, 085318.
18. C. Zhang, C. Chuu, X. Ren, M. Li, L. Li, C. Jin, M. Chou and C. Shih, *Science Advances*, 2017, **3**, e1601459.
19. M. Bernardi, M. Palummo and J. Grossman, *Nano Letters*, 2013, **13**, 3664-3670.
20. J. Kang, S. Tongay, J. Zhou, J. Li and J. Wu, *Applied Physics Letters*, 2013, **102**, 012111.
21. C. Gong, H. Zhang, W. Wang, L. Colombo, R. Wallace and K. Cho, *Applied Physics Letters*, 2013, **103**, 053513.
22. H. Terrones, F. Lopez-Urias and M. Terrones, *Scientific Reports*, 2013, **3**, 1549.
23. J. He, K. Hummer and C. Franchini, *Physical Review B*, 2014, **89**, 075409.
24. N. Lu, H. Guo, L. Li, J. Dai, L. Wang, W. Mei, X. Wu and X. Zeng, *Nanoscale*, 2014, **6**, 2879-2886.
25. F. Ceballos, M. Bellus, H. Chiu and H. Zhao, *Acs Nano*, 2014, **8**, 12717-12724.
26. N. Lu, H. Guo, L. Wang, X. Wu and X. Zeng, *Nanoscale*, 2014, **6**, 4566-4571.
27. J. Wang, R. Namburu, M. Dubey and A. M. Dongare, *Scientific Reports*, 2018, **8**, 9439.
28. Y. Wang, Z. Wang, W. Yao, G. Liu and H. Yu, *Physical Review B*, 2017, **95**, 115429.
29. S. Huang, X. Ling, L. Liang, J. Kong, H. Terrones, V. Meunier and M. Dresselhaus, *Nano Letters*, 2014, **14**, 5500-5508.

30. K. Wang, B. Huang, M. Tian, F. Ceballos, M. Lin, M. Mahjouri-Samani, A. Boulesbaa, A. Poretzky, C. Rouleau, M. Yoon, H. Zhao, K. Xiao, G. Duscher and D. Geohegan, *ACS Nano*, 2016, **10**, 6612-6622.
31. S. Carr, D. Massatt, S. Fang, P. Cazeaux, M. Luskin and E. Kaxiras, *Physical Review B*, 2017, **95**, 075420.
32. M. Wu, X. Qian and J. Li, *Nano Letters*, 2014, **14**, 5350-5357.
33. B. Hunt, J. Sanchez-Yamagishi, A. Young, M. Yankowitz, B. LeRoy, K. Watanabe, T. Taniguchi, P. Moon, M. Koshino, P. Jarillo-Herrero and R. Ashoori, *Science*, 2013, **340**, 1427-1430.
34. L. Ponomarenko, R. Gorbachev, G. Yu, D. Elias, R. Jalil, A. Patel, A. Mishchenko, A. Mayorov, C. Woods, J. Wallbank, M. Mucha-Kruczynski, B. Piot, M. Potemski, I. Grigorieva, K. Novoselov, F. Guinea, V. Fal'ko and A. Geim, *Nature*, 2013, **497**, 594-597.
35. C. Dean, L. Wang, P. Maher, C. Forsythe, F. Ghahari, Y. Gao, J. Katoch, M. Ishigami, P. Moon, M. Koshino, T. Taniguchi, K. Watanabe, K. Shepard, J. Hone and P. Kim, *Nature*, 2013, **497**, 598-602.
36. R. Gorbachev, J. Song, G. Yu, A. Kretinin, F. Withers, Y. Cao, A. Mishchenko, I. Grigorieva, K. Novoselov, L. Levitov and A. Geim, *Science*, 2014, **346**, 448-451.
37. F. Wu, T. Lovorn and A. MacDonald, *Physical Review Letters*, 2017, **118**, 147401.
38. Q. Tong, H. Yu, Q. Zhu, Y. Wang, X. Xu and A. Yao, *Nature Physics*, 2017, **13**, 356-362.
39. Y. Cao, V. Fatemi, S. Fang, K. Watanabe, T. Taniguchi, E. Kaxiras and P. Jarillo-Herrero, *Nature*, 2018, **556**, 43-+.
40. E. Mele, *Physical Review B*, 2010, **81**, 161405(R).
41. P. Moon and M. Koshino, *Physical Review B*, 2013, **87**, 205404.
42. A. Nayak, S. Bhattacharyya, J. Zhu, J. Liu, X. Wu, T. Pandey, C. Jin, A. Singh, D. Akinwande and J. Lin, *Nature Communications*, 2014, **5**, 3731.
43. S. PLIMPTON, *Journal of Computational Physics*, 1995, **117**, 1-19.
44. A. Ostadhossein, A. Rahnamoun, Y. Wang, P. Zhao, S. Zhang, V. Crespi and A. van Duin, *Journal of Physical Chemistry Letters*, 2017, **8**, 631-640.
45. J. Soler, E. Artacho, J. Gale, A. Garcia, J. Junquera, P. Ordejon and D. Sanchez-Portal, *Journal of Physics-Condensed Matter*, 2002, **14**, 2745-2779.
46. S. Huang, L. Liang, X. Ling, A. Poretzky, D. Geohegan, B. Sumpter, J. Kong, V. Meunier and M. Dresselhaus, *Nano Letters*, 2016, **16**, 1435-1444.
47. R. Suzuki, M. Sakano, Y. Zhang, R. Akashi, D. Morikawa, A. Harasawa, K. Yaji, K. Kuroda, K. Miyamoto, T. Okuda, K. Ishizaka, R. Arita and Y. Iwasa, *Nature Nanotechnology*, 2014, **9**, 611-617.
48. T. Jiang, H. Liu, D. Huang, S. Zhang, Y. Li, X. Gong, Y. Shen, W. Liu and S. Wu, *Nature Nanotechnology*, 2014, **9**, 825-829.
49. J. Jiang, Z. Qi, H. Park and T. Rabczuk, *Nanotechnology*, 2013, **24**, 43.
50. D. Lloyd, X. Liu, J. Christopher, L. Cantley, A. Wadehra, B. Kim, B. Goldberg, A. Swan and J. Bunch, *Nano Letters*, 2016, **16**, 5836-5841.
51. H. Guo, N. Lu, L. Wang, X. Wu and X. Zeng, *Journal of Physical Chemistry C*, 2014, **118**, 7242-7249.



**a general moiré-templated nanoscale morphology engineering method**

150x83mm (300 x 300 DPI)